Annals of Biomedical Engineering, Vol. 33, No. 11, November 2005 (© 2005) pp. 1640–1652
DOI: 10.1007/s10439-005-7410-3

A Predictive Model of Therapeutic Monoclonal Antibody Dynamics and Regulation by the Neonatal Fc Receptor (FcRn)

GREGORY Z. FERL,[1] ANNA M. WU,[2] and JOSEPH J. DISTEFANO III[1]

[1]Biocybernetics Laboratory, Departments of Computer Science and Medicine and Biomedical Engineering Interdepartmental Program, University of California, Los Angeles and [2]Department of Molecular and Medical Pharmacology, Crump Institute for Molecular Imaging, UCLA School of Medicine

(Received 4 May 2005; accepted 14 July 2005)

Abstract—We constructed a novel physiologically-based pharmacokinetic (PBPK) model for predicting interactions between the neonatal Fc receptor (FcRn) and anti-carcinoembryonic antigen (CEA) monoclonal antibodies (mAbs) with varying affinity for FcRn. Our new model, an integration and extension of several previously published models, includes aspects of mAb-FcRn dynamics within intracellular compartments not represented in previous PBPK models. We added mechanistic structure that details internalization of class G immunoglobulins by endothelial cells, subsequent FcRn binding, recycling into plasma of FcRn-bound IgG and degradation of free endosomal IgG. Degradation in liver is explicitly represented along with the FcRn submodel in skin and muscle. A variable tumor mass submodel is also included, used to estimate the growth of an avascular, necrotic tumor core, providing a more realistic picture of mAb uptake by tumor. We fitted the new multiscale model to published anti-CEA mAb biodistribution data, i.e. concentration-time profiles in tumor and various healthy tissues in mice, providing new estimates of mAb-FcRn related kinetic parameters. The model was further validated by successful *prediction* of $F(\mathrm{ab}')_2$ mAb fragment biodistribution, providing additional evidence of its potential value in optimizing intact mAb and mAb fragment dosing for clinical imaging and immunotherapy applications.

Keywords—Monoclonal Antibodies, Neonatal Fc receptor, Mathematical model, Animal Models, Pharmacokinetics.

INTRODUCTION

Therapeutic Monoclonal Antibodies[11,30]

Monoclonal antibodies (mAbs) represent a major advance in cancer therapy, often allowing a patient to undergo treatment with reduced or minimal impact to healthy tissues, in contrast to chemotherapy and radiotherapy. The number of clinical trials related to mAbs increased sharply during the early 1990s (PubMed literature search, not shown), culminating with the approval of rituximab (Rituxan$^{\mathrm{TM}}$) in 1997 (U.S.) for the treatment of non-Hodgkin's lymphoma (NHL). Rituximab targets and mediates the destruction of tumor cells via CD20, a transmembrane protein present only on lymphoma cells and the B lymphocytes from which they are derived.[37] Trastuzumab (Herceptin$^{\mathrm{TM}}$) was approved for use in the U.S. the following year, and targets HER-2/*neu*, a cell surface protein associated with aggressive tumor growth, overexpressed in 20–30% of breast cancers.[41] Other mAbs have since been approved at an increasing rate and include agents for the treatment of acute myelogenous leukemia [Gemtuzumab ozogamicin (Mylotarg$^{\mathrm{TM}}$)], chronic lymphocytic leukemia [Alemtuzumab (Campath$^{\mathrm{TM}}$)] and colorectal cancer [Cetuximab (Erbitux$^{\mathrm{TM}}$) and Bevacizumab (Avastin$^{\mathrm{TM}}$)]. Also, additional mAbs used for radioimmunotherapy of NHL have recently been approved [Ibritumomab tiuxetan (Zevalin$^{\mathrm{TM}}$) and Tositumomab (Bexxar$^{\mathrm{TM}}$)].

Most currently approved mAbs are only effective against specific types of cancers, but some show potential as broader anti-tumor agents. Bevacizumab, approved in early 2004, targets the vascular endothelial growth factor (VEGF), a ligand for the VEGF receptor (VEGFR), expressed by budding endothelial cells during angiogenesis (blood vessel growth).[30] VEGF is released by tumor cells to stimulate tumor vascularization and growth; some tumor cells may also express VEGFR in order to receive proliferation signals in an autocrine/paracrine manner,[14] so that blocking VEGF function with Bevacizumab can potentially inhibit tumor cell growth directly, in addition to blocking angiogenesis. mAbs also have treatment applications beyond cancer, e.g., use of rituximab for treatment of a variety of autoimmune disorders.[35]

Neonatal Fc Receptor (FcRn)[19,45]

In 1964, Brambell and coworkers proposed that class G immunoglobulin (IgG) elimination is mediated by a saturable rescue mechanism.[8] They based this idea on

---

Address correspondence to Joseph J. DiStefano III, Department of Computer Science, 4711 Boelter Hall, Los Angeles, CA 90095-1596. Electronic mail: joed@cs.ucla.edu

0090-6964/05/1100-1640/1 © 2005 Biomedical Engineering Society

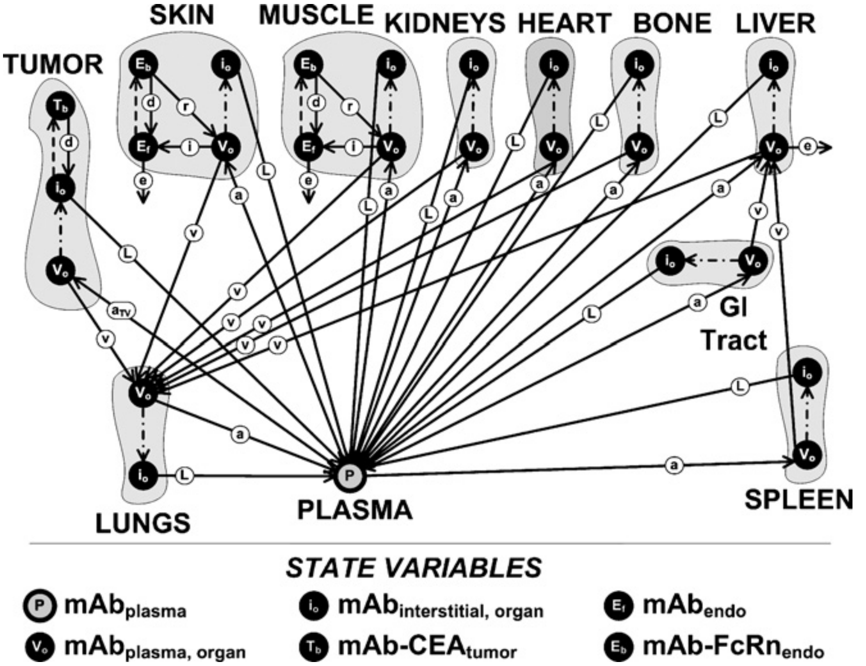

FIGURE 1. PBPK model of monoclonal antibody biodistribution. Schematic of our augmented PBPK model used to both describe intact mAb biodistribution (Model B) and predict *F*(ab′)$_2$ biodistribution (Model C). Flux arrows labeled with a single letter represent linear, time-invariant mass transfer via: a: Arterial blood flow; v: Venous blood flow; L: Lymph flow; e: Elimination from body; i: Internalization by endothelial cells; r: Recycling from endothelial cell back into plasma and d: Dissociation from FcRn or CEA. The subscript TV indicates linear, time-varying mass transfer. Nonlinear mass fluxes include mass action based antibody binding (- - -) and antibody extravasation described by the two-pore macromolecule extravasation submodel[38] (– · –) shown in Fig. 2. See Appendix for model equations and parameter values.

experimental data showing that the apparent half-life of IgG decreased as total IgG concentration increased,[15] and proposed a simple, empirical model describing the effect of this hypothetical Brambell receptor on IgG half-life kinetics in mice: $t_{1/2} = C \ln 2/(a(C - b))$, where $a = 0.34$, $b = 2.5$ and C is total IgG concentration in mg/ml.

In 1972, an Fc receptor was identified that mediates the transfer of IgG from mother's milk to intestinal blood in neonatal rats[26] via the immunoglobulin Fc region, thereafter called the neonatal Fc receptor (FcRn). FcRn was later characterized as a dimer that transports IgG via a pH-dependent mechanism of association and dissociation,[39] and was also shown to mediate materno-fetal transfer of IgG across the placenta in pregnant mice.[23] The X-ray crystallographic structure of the molecule revealed that FcRn is similar to the MHC class-I molecule, consisting of a three-domain alpha subunit coupled with β-2-microglobulin;[10] the portion of FcRn analogous to the MHC I peptide-binding groove is occluded by an α-helix.

In 1996, FcRn was identified as the hypothetical Brambell receptor,[18,24,27] and further studies identified key residues in both the Fc region of IgG[29] and FcRn[47] capable of attenuating Fc–FcRn binding when mutated. Direct evidence of the role of FcRn in perinatal IgG transport and FcRn-mediated IgG degradation was recently reported in FcRn knockout mice.[40] It is believed that FcRn is expressed primarily within muscle and skin endothelium[7,18] of adult mice and humans, and rescues IgGs from degradation by diverting intracellular, FcRn bound IgG away from the lysosomal degradation pathway.[34]

Physiologically Based Pharmacokinetic Models[17,33,46]

Mathematical biomodels structured according to physiological connectivity are common in many areas of life science.[28,36] This approach has recently been applied to drug kinetics with the designation 'physiologically-based pharmacokinetic (PBPK) modeling.'

PBPK models typically include physiological parameters, such as blood flow rates and organ volumes, along with drug-dependent parameters, such as rates of drug binding and metabolism. Organs are typically represented by interacting pools (with linear or nonlinear components), representing vascular, interstitial and/or intracellular spaces, among others, as in Fig. 1. The lungs are usually included, with efferent organ plasma flux of drug flowing to the systemic circulation (central plasma pool) via the pulmonary circulation (lungs). Pharmacodynamic components, mechanistic or otherwise, may also be included. Physiologically based modeling has been facilitated by a concerted effort to amass measured physiological parameters from various mammalian species (especially mouse, rat and human) for use in the construction of PBPK models.[9]

Application of PBPK Modeling to Monoclonal Antibody Kinetics

The PBPK modeling approach has previously been applied to studies of the biodistribution of intact anti-carcinoembryonic antigen (CEA) mAbs and their fragments [Fab, $F(ab')_2$] in mice[4] (designated Model A here). Based on an earlier model,[12] Model A was initially developed from mouse data, and allometric scaling[13] yielded specific parameters for a human PBPK model.[3] The two-pore theory of macromolecule extravasation[38] is a key feature of both models[3,4] and is used to describe the flux of immunoglobulins from capillary to interstitial space (see Fig. 2).

We augment Model A[4] in several ways. First, our new model, designated Model B, includes an FcRn submodel based on experimental data that suggests inclusion of intracellular compartments within skin and muscle endothelium[7,18,34] for representing mAb half-life regulation via FcRn. The FcRn submodel can be used to predict the kinetic properties and biodistribution of different mAbs and mAb fragments with varying affinities for FcRn. Second, we removed the kidney leak utilized in Model A[4] as the sole site of mAb elimination, since very little mAb elimination is believed to occur there,[48] and added a first-order leak to the liver pool, where a significant amount of mAb degradation takes place.[16,48] Finally, we developed a variable tumor mass submodel that describes growth of both vascular and avascular (necrotic) regions of the tumor over time (see Methods), based on studies reported by Williams *et al.*[49] that suggest a necrotic tumor core develops in the animal/tumor model used to produce data utilized in our study, reducing the fraction of total tumor accessible to blood and mAbs.

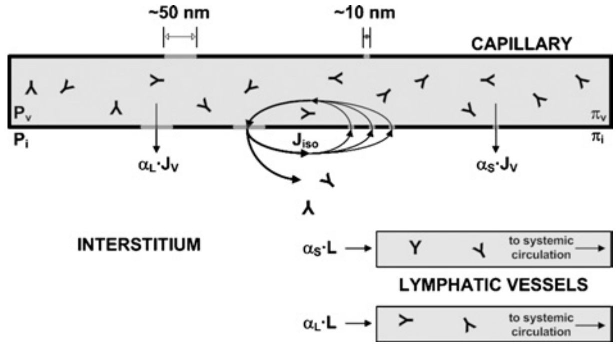

FIGURE 2. Two-pore model of antibody extravasation.[38] The capillary is modeled as having two pore types, large and small. A large number of small pores (~10 nm) exist in the capillary along with a lesser number of large pores (~50 nm), through which macromolecules can pass by either convection or diffusion. Fluid recirculation occurs at a rate J_{iso}, with the small pores acting as a filter, trapping large molecules in the interstitial space. Excess fluid flux into the interstitial space occurs at a rate J_V and is taken up by the lymphatic system at a rate L (which is equal to J_V). α_L and α_S are the fractions of bulk fluid passing through large and small pores, respectively ($\alpha_L + \alpha_S = 1$). See Appendix for the two-pore model equations.

We compare Model B, first with Model A, plus two variants: Model $B_{\text{constant tumor mass}}$—same as Model B, but with a constant tumor mass in place of the variable tumor mass submodel; and Model $B_{\text{linear leaks}}$—same as Model B, but with first-order (linear) leaks emanating from the vascular compartments of skin and muscle in place of the 2-compartment FcRn submodels. Finally, we extend Model B to Model C—our novel PBPK model for the $F(ab')_2$ *fragment*, which also includes the FcRn submodel and variable tumor mass submodel; $k_{\text{on,FcRn}}$ is set to zero within the FcRn submodel, effectively removing compartment $\mathbf{E_b}$ (Fig. 1). Table 1 summarizes the models and their attributes.

METHODS

Model Simulations and Parameter Estimation Methods

Parameter values for our new model were obtained as follows, 51 were available from the original model[4] and 13 others were gathered from additional literature.[6,9,22,32,38,47,49,50] The remaining 15 were estimated (see Results) from experimental data.[50] These are given in the Appendix and in Table 2.

Models were implemented and parameters were estimated using SAAM II,[2] fitting each model simultaneously to all biodistribution data using weighted least squares optimization, first using the relative data weighting scheme[5] provided in SAAM II. Plasma data weights were then increased by an order of magnitude, since plasma measurements are more precise than raw organ tissue measurements, providing better overall fits.

Biological Data for Fitting the Models

Model B was fitted to mouse biodistribution data reported in[50] and residual carcass data generously provided by Larry Williams, City of Hope. Briefly, the authors studied the pharmacokinetics and biodistribution in tumor, blood, liver, spleen, kidney, lung, stomach, bowel, bone and carcass of a chimeric anti-CEA IgG_1 monoclonal antibody (cT84.66), plus four of its fragments: 120 kDa $F(ab')_2$, 80 kDa minibody, 55 kDa diabody, 28 kDa scFv. Female nude mice were flank injected with human colorectal tumor LS174T (ATCC CL 188) cells. The tumor cell population was allowed to grow for 10 days prior to a second injection, antibody labeled with ^{123}I, ^{125}I or ^{131}I. Between four and nine mice were killed at each of the following timed data points: 0, 2, 3, 6, 12, 18, 24, 48, 72 h ($F(ab')_2$) and 0, 6, 13, 24, 48, 72, 96, 120, 168 h (intact mAb). The organs noted were excised, weighed and counted for remaining

TABLE 1. Mathematical models used in this study.

Model	Variable tumor mass submodel	FcRn submodel	mAb described
Model A (Baxter *et al.*, 1994)	No	No	Intact mAb
Model B	Yes	Yes	Intact mAb
Model $B_{\text{linear leaks}}$	Yes	No	Intact mAb
Model $B_{\text{constant tumor mass}}$	No	Yes	Intact mAb
Model C	Yes	Yes	$F(\mathrm{ab}')_2$ mAb fragment

radioactivity. We used only ^{131}I-labeled intact mAb biodistribution data from these assays for fitting Model B, and $F(\mathrm{ab}')_2$ fragment data was compared to our predictions using Model C.

FcRn Submodel

The FcRn mechanism is depicted as a nonlinear 2-compartment model, with state variables $\mathbf{E}_\mathrm{f}$ (unbound mAb) and $\mathbf{E}_\mathbf{b}$ (FcRn-bound mAb) within endothelial cells in Fig. 1. Flux i represents linear transfer of mAb from organ vascular space to endosomes via nonspecific bulk fluid uptake by endothelial cells. Flux e represents linear degradation of unbound mAb. The dashed line represents binding of mAb to FcRn (Eqs. A.9(a)–A.9(c), Appendix). Flux d represents linear dissociation of mAb from FcRn and flux r represents transport of FcRn-bound mAb from the endosome back into plasma.

Estimation of Unbound FcRn Concentration

The concentration of unbound FcRn was estimated from the aforementioned study,[8] where IgG half-life was measured at increasing total IgG concentrations in BALB/c mice and plotted as $t_{1/2,\mathrm{IgG}}$ vs. [IgG]. We fitted this data (not shown) using the program W^{3}DIMSUM (http://biocyb.cs.ucla.edu/dimsum), an expert system for multiexponential modeling that fits 1-, 2-, 3- and 4-exponential functions to any data set. The fitted 2-exponential function, $t_{1/2,\mathrm{IgG,fast}} = 6.76\,e^{-0.507[\mathrm{IgG}]} + 4.00\,e^{-0.0244[\mathrm{IgG}]}$, had the best fit with a weighted residual sum of squares (WRSS) of 12.7, compared to WRSS values of 20.1, 46.1, and 22.1 for the 1-, 3- and 4–exponential model fits. We assume that the fast component of the 2–exponential curve ($6.76\,e^{-0.507[\mathrm{IgG}]}$) represents FcRn saturation and the slow component ($4.00\,e^{-0.0244[\mathrm{IgG}]}$) represents other mechanisms of IgG kinetic regulation. The fast component indicates that FcRn is saturated at a total IgG concentration of $\approx$7 mg/ml. Since the basal concentration of total IgG in 6 week old nude mice is reported to be $\approx$1 mg/ml,[32] we estimated that the FcRn binding sites will saturate at an IgG concentration of about 6 mg/ml (4×10^{-8} mol/ml); this number is used as the effective concentration of free FcRn binding sites prior to injection of the intact mAb.

Estimation of Total Tumor Antigen Concentration

Assume CEA density[6] $\approx 5 \times 10^5$ CEA/cell. Assume cell density $\approx 10^8$ cells/g. CEA density $\times$ cell density $\approx 5 \times 10^{13}$ CEA/g $= 8.30 \times 10^{-11}$ mol/g $\cong 8.30 \times 10^{-11}$ mol/ ml.

Estimation of Total Endosomal Volume

Endothelial cell endosomes are treated as an extension of the organ microvasculature such that the *total concentration* of IgG (FcRn-bound and unbound) within the endosome is always equal to the concentration of IgG in the organ microvasculature (Eq. A.9(c)).

Variable Tumor Mass Submodel

The variable tumor mass submodel is based on *in vivo* measurements of total tumor mass (provided by Larry Williams, City of Hope), which were fitted with the Gompertz equation,[42] (Fig. 3, solid lines) using Prism (GraphPad Software for Science, San Diego, CA). The equation was attenuated based on studies of perfusable tumor mass as a function of total tumor size in mice, where the authors[49] parameterize a power function (uptake $= B \times \mathrm{mass}^A$) that relates antibody uptake by tumor (%ID/g) to total tumor mass. Based on *in vivo* data, using the same antibody-tumor system described in Williams *et al.*,[50] the authors estimate that the power function has values of $B = 18.1$ and $A = -0.38$. We used the parameterized power function to estimate perfusable tumor mass as a function of total tumor mass (Eqs. A.8(b) and A.8(c)).

Estimation of Hepatic Degradation Rate

A liver degradation rate was chosen that allows liver to account for approximately 40% of total degraded intact mAb.[48] Since we are neglecting degradation in other organs (spleen, tumor, etc), the 40% value accounts for liver plus all other degradation sites not located in skin or muscle.

RESULTS

As a preliminary validation of our model implementation, we first successfully reproduced the primary blood

TABLE 2. Model parameters and fitted parameter estimates.

Parameter	Units	Description	Source	Value $\times 10^{-4}$	%CV
Physiological parameters					
$J_{\text{iso, organ, sp}}$	$\text{ml min}^{-1}\text{ g}^{-1}$	Fluid recirculation flow rate for each organ	Fitted	tumor: 6.8	4
				GI tract: 3.0	317
				bone: 0.52	31
				kidney: 2.3	59
				liver: 13.1	866
				lung: 6.6	25
Q_{organ} and $Q_{\text{tumor, sp}}$	ml min^{-1} $\text{ml min}^{-1}\text{ g}^{-1}$	Plasma flow rate to organ and tumor	Baxter *et al.* (1994)		
$\text{Mass}_{\text{organ}}$	g	Mass of organ	Baxter *et al.* (1994)		
$\text{Mass}_{\text{tumor}}$	g	Mass of tumor	Williams *et al.* (2001)		
$\text{Mass}_{\text{tumor, perfuasble}}$	g	Perfusable tumor mass	Williams *et al.* (1988)		
$k_{\text{on, CEA}}$	$\text{mol mol}^{-1}\text{ min}^{-1}$	Association rate for antibody/antigen binding	Hefta *et al.* (1998)		
$k_{\text{off, CEA}}$	min^{-1}	Dissociation rate for antibody/antigen binding	Hefta *et al.* (1998)		
$L_{\text{organ, sp}}$	$\text{ml min}^{-1}\text{ g}^{-1}$	Lymph flow rate for each organ	Fitted	GI tract: 23	307
				spleen: 1.1	19
				bone: 3.0	32
				liver: 65	827
				kidney: 14	64
				lung: 8.5	29
V_{plasma}	ml	Plasma volume	Brown *et al.* (1997)		
$V_{\text{v, organ}}$ and $\text{V}_{\text{v, tumor, sp}}$	ml ml g^{-1}	Volume of organ and tumor vascular space	Baxter *et al.* (1994)		
$V_{\text{i,organ}}$ and $\text{V}_{\text{i, tumor, sp}}$	ml ml g^{-1}	Volume of organ and tumor interstitial space	Baxter *et al.* (1994)		
α_{L} and α_{S}	—	Fraction of extravasation occuring via large and small pores	Rippe and Haraldsson (1994)		
FcRn_{tot}	mol ml^{-1}	Total FcRn concentration	Estimated from Brambell *et al.* (1964)		
$B_{\text{max, sp}}$	mol ml^{-1}	Tumor antigen concentration	Berk *et al.* (1997)		
$k_{\text{deg, liver}}$	ml min^{-1}	Degradation rate of mAb in liver	Estimated from Waldmann *et al.* (1969)		
Drug dependent parameters					
σ_{L} and σ_{S}	—	Osmotic reflection coefficient for large and small pores	Baxter *et al.* (1994)		
$\text{PS}_{\text{L, organ}}\cdot\text{PS}_{\text{s, organ}}$	$\text{ml min}^{-1}\text{ g}^{-1}$	Permeability-surface area product (large and small pores)	Baxter *et al.* (1994)		
$k_{\text{on, FcRn}}$	$\text{ml mol}^{-1}\text{ min}^{-1}$	Binding constant for IgG-FcRn interaction	Vaughn and Bjorkman (1997)		
$k_{\text{off, FcRn}}$	min^{-1}	Dissociation constant for IgG-FcRn interaction	Vaughn and Bjorkman (1997)		
FcRn submodel parameters					
$k_{\text{int, FcRn}}$	min^{-1}	Nonspecific internalization rate of free mAb	Fitted	96	12
$k_{\text{rec, FcRn}}$	min^{-1}	Recycling rate of FcRn bound mAb	Fitted	35	14

TABLE 2. Continued.

Parameter	Units	Description	Source	Value $\times 10^{-4}$	%CV
$k_{\text{deg, FcRn}}$	min^{-1}	Degradation rate of unbound endosomal mAb	Fitted	6127	4

Note. Best estimates and percent coefficients of variation (%CV) are shown for unknown parameters. Remaining parameters were obtained from the literature, as noted, and are given in the Appendix. Each organ has a different best estimate value for J_{iso} and L, shown in the two rightmost columns. Best estimates for k_{int}, k_{deg} and k_{rec} are also shown. For organs with no experimental data available, J_{iso} and L values from Baxter *et al.*[4] were used. Lymph flow rate for tumor is assumed to be zero.[25] $J_{\text{iso, spleen}}$ is most likely unidentifiable and was set to 2×10^{-7}.

and tumor simulation results from,[4] by stripping Model B of all augmentations (resulting in Model A) and using their published parameter values.[4] We then explored the new model and its variants.

Model B Fitted to Intact mAb Biodistribution Data and Model B Parameter Estimates

We estimated 15 unknown model parameters ($J_{\text{iso, tumor, sp}}$, $J_{\text{iso, GI, sp}}$, $J_{\text{iso, bone, sp}}$, $J_{\text{iso, kidney, sp}}$, $J_{\text{iso, liver, sp}}$, $J_{\text{iso, lung, sp}}$, $L_{\text{GI, sp}}$, $L_{\text{spleen, sp}}$, $L_{\text{bone, sp}}$, $L_{\text{liver, sp}}$, $L_{\text{kidney, sp}}$, $L_{\text{lung, sp}}$, k_{int}, k_{deg} and k_{rec}) from the data, with model B fitting the experimental data as shown in Fig. 4. The dotted line represents the fitted simulation results for each organ, shown with the corresponding experimental data[50] (open circles). Table 2 provides optimized parameter estimates and their percent coefficients of variation (%CV), which range from 4–866%. The parameter estimates for the FcRn submodel are among those with the lowest variability: $k_{\text{int}} \approx 0.01 \pm 0.001$ (±SD), $k_{\text{deg}} \approx 0.6 \pm 0.03$ and $k_{\text{rec}} \approx 0.003 \pm 0.0005\,\text{min}^{-1}$; these correspond to fluxes i, d and r, respectively, in the skin and muscle pools of Fig. 1.

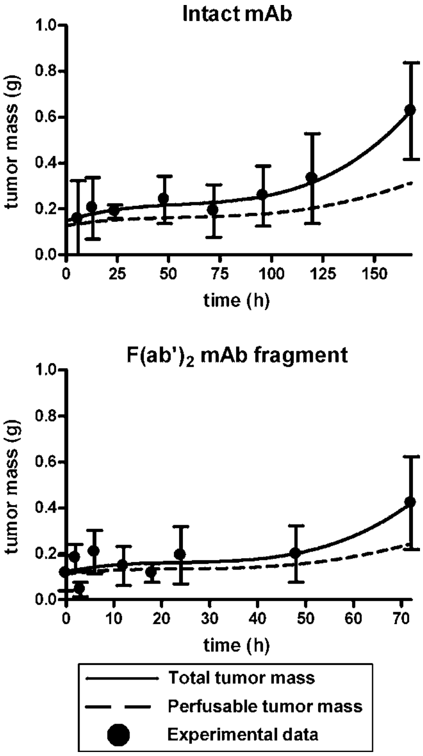

FIGURE 3. Variable tumor mass submodel for Model B, $B_{\text{linear leaks}}$ and Model C. Tumor growth models based on unpublished data (provided by L. Williams) from the *intact* mAb (used in Model B) and *F*(ab′)$_2$ (used in Model C) experiments reported in Williams *et al.*[50] Each graph compares total tumor mass, described by the fitted Gompertz equation (—), to estimated perfusable tumor mass (···), which was calculated based on data from a previous study by Williams *et al.*[49]

Prediction of F(ab′)$_2$ Fragment Biodistribution Using Model C

To exercise our new model, we predicted the biodistribution of cT84.66 $F(\text{ab}')_2$ antibody fragments, after making the following changes to the parameters of Model B. First, the on-rate ($k_{\text{on, FcRn}}$) for the IgG-FcRn interaction was set to zero based on the assumption that the $F(\text{ab}')_2$ fragment does not bind FcRn, due to absence of an Fc region. The osmotic reflection coefficients and permeability-surface area coefficients (σ_{S}, σ_{L}, PS_{S} and PS_{L}), which characterize resistance to drug extravasation via diffusion and convection, were changed from intact mAb values to $F(\text{ab}')_2$ values[4] (see Appendix). The tumor growth data from the $F(\text{ab}')_2$ biodistribution experiments[50] was used. In Fig. 4, the solid line represents $F(\text{ab}')_2$ biodistribution predicted by Model C, shown with the corresponding experimental data[50] (solid circles). Visually, the matches between predictions and data are quite good for all 9 data sets.

Model B Fits the Data Better than Model A, Model $B_{\text{linear leaks}}$ and Model $B_{\text{constant tumor mass}}$

We also fitted Model A[4] simultaneously to all of the cT84.66 intact mAb biodistribution data,[50] to obtain an objective measure of the quality of the two models, A and B, fitted in the same manner to the same set of data. The Akaike information criterion (AIC),[1] a metric used in model discrimination, was 19.4 for Model A and 6.1 for Model B,

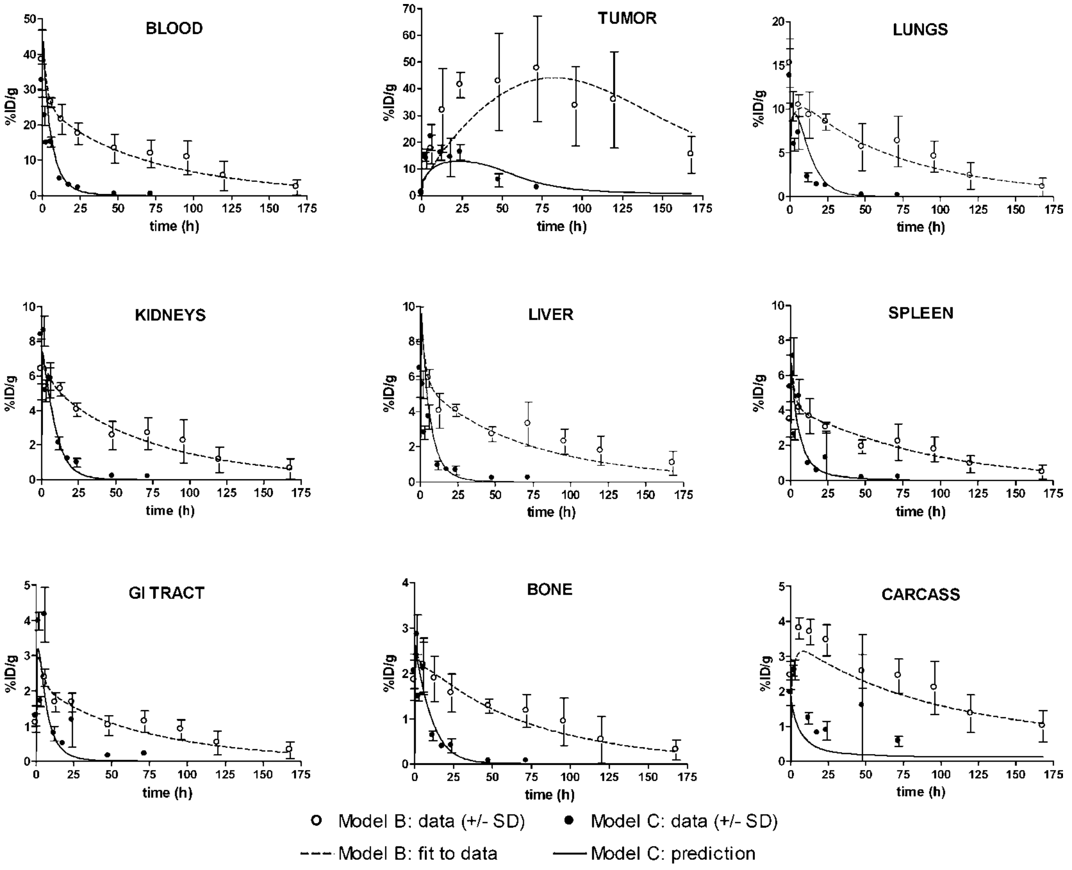

FIGURE 4. Fitted and predicted Model B and C simulations for intact mAb and the *F*(ab′)$_2$ *fragment* (%ID/g vs. time). The dotted lines in each panel represent Model B fitted to biodistribution data[50] (open circles, mean ± SD of four mice) of an intact anti-CEA mAb in tumor bearing nude mice. The solid lines represent Model C predictions of the biodistribution of the *F*(ab′)$_2$ antibody *fragment* data (solid circles, mean ± SD of four to nine mice). Model C was simulated by altering the parameters of Model B based on known differences in the kinetics of the two molecules (see Appendix for drug specific parameters).

computed over tumor and all organs. A lower AIC indicates a better fit of model to data.

Model $B_{\text{constant tumor mass}}$ fitted the tumor curve poorly (Fig. 5), resulting in an overall AIC value of 8.4. Model $B_{\text{linear leaks}}$ fitted the tumor data better, but not as well overall, resulting in an AIC of 33.7 computed over all organs. The same data weighting scheme was used for all fits.

Tumor Growth and FcRn Submodels Improve Fit to Tumor and Residual Carcass Data

As clearly illustrated in Fig. 5, the two models that assume a constant tumor mass in place of the variable tumor mass submodel [Model A ($\text{AIC}_{\text{tumor}} = 2.2$) and Model $B_{\text{constant tumor mass}}$ ($\text{AIC}_{\text{tumor}} = 2.4$)] did not fit the tumor data as well as the two models that utilize the tumor growth model [Model B ($\text{AIC}_{\text{tumor}} = 1.6$) and Model $B_{\text{linear leaks}}$ ($\text{AIC}_{\text{tumor}} = 1.1$)]. Similarly, the two models that lack the FcRn submodel [Model A ($\text{AIC}_{\text{carcass}} = 4.8$) and Model $B_{\text{linear leaks}}$ ($\text{AIC}_{\text{carcass}} = 8.1$)] did not fit residual carcass data as well as the two models that include the FcRn submodel [Model B ($\text{AIC}_{\text{carcass}} = 0.71$) and Model $B_{\text{constant tumor mass}}$ ($\text{AIC}_{\text{carcass}} = 0.58$)] (see Fig. 5 and Table 1).

Model B Drug Distribution Predictions Within Organ Pool Compartments

Using Model B, the predicted concentration-time profiles for experimentally unmeasured individual compartments within muscle, tumor and kidney submodels are shown in Fig. 6. These simulations predict that about half of intact antibody within muscle is bound to FcRn within endothelial cell endosomes, while virtually all antibody within tumor is bound to the tumor marker CEA. Antibody within the two-compartment organ pools (kidney, heart, bone, liver, spleen, lung and GI tract) is predicted to have an approximate 2:1 vascular:interstitial distribution after reaching maximum interstitial antibody concentration at about 11 h, coinciding with previously published experimental results showing that vascular—interstitial equilibrium of antibody requires 12–24 h.[44]

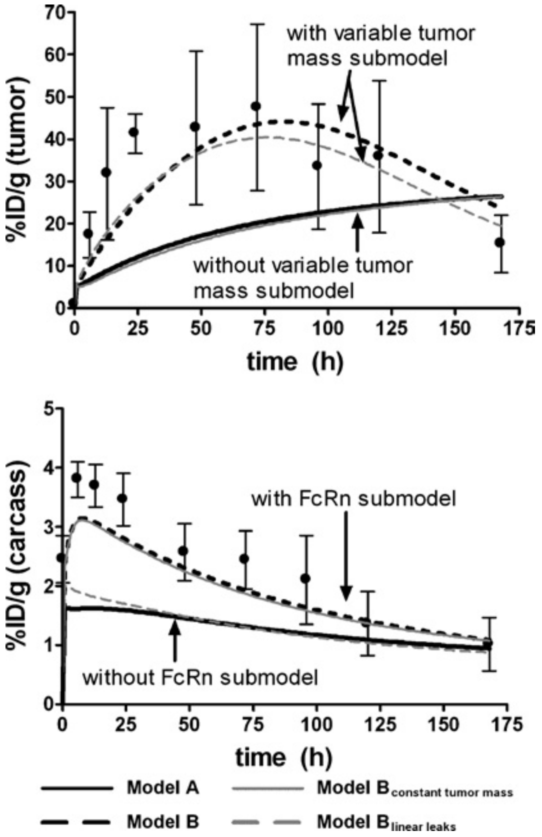

FIGURE 5. Comparison of tumor and carcass concentration-time profiles generated by Models A, B, $B_{\text{linear leaks}}$ and $B_{\text{constant tumor mass}}$. Illustrates improved fit to tumor data via incorporation of the variable tumor mass submodel (Models B and $B_{\text{linear leaks}}$ vs. Models A and $B_{\text{constant tumor mass}}$) and the improved fit to residual carcass data when the FcRn submodel is utilized (Models B and $B_{\text{constant tumor mass}}$ vs. Models A and $B_{\text{linear leaks}}$). See Table 1 for model descriptions.

DISCUSSION

Our model modifies and extends the previously published model structure[4] in several ways. First, we added two compartments to the skin and muscle pools, where a significant number of Fc-FcRn interactions are believed to occur.[7,18] We believe these newer developments are needed in the model, to further understanding of IgG regulation. Second, we removed the kidney leak utilized in[4] as the sole site of mAb elimination, since very little mAb elimination is believed to occur there,[48] and added a first order leak to the liver pool, where a significant amount of mAb degradation takes place.[16,48] Finally, because tumor mass increased sevenfold during the 168 h study,[50] we also included a variable tumor mass submodel based on measurements of tumor mass at each biodistribution time point.

As illustrated by Fig. 5 and Table 1, the model that contains the variable tumor mass submodel without the FcRn submodel (Model $B_{\text{linear leaks}}$) fits tumor data much better than the model that contains the FcRn submodel without the variable tumor mass submodel (Model $B_{\text{constant tumor mass}}$), indicating that the improved tumor data fit is the result of a more accurate mechanistic description of mAb uptake by tumor rather than added dynamics from both the tumor and FcRn submodels. Likewise, Model $B_{\text{constant tumor mass}}$ fits carcass data much better than Model $B_{\text{linear leaks}}$, suggesting that the improved fit to carcass data is the result of a more accurate mechanistic description of mAb kinetics in skin, muscle and bone via the FcRn submodel. Our simulations predict that perfusable tumor mass remains relatively constant over the course of the experiment (Fig. 2), even when total tumor mass increases considerably. However, our variable tumor mass submodel provides a more accurate description of antibody-tumor kinetics (Fig. 5), by enhancing the tumor measurement model, which depicts

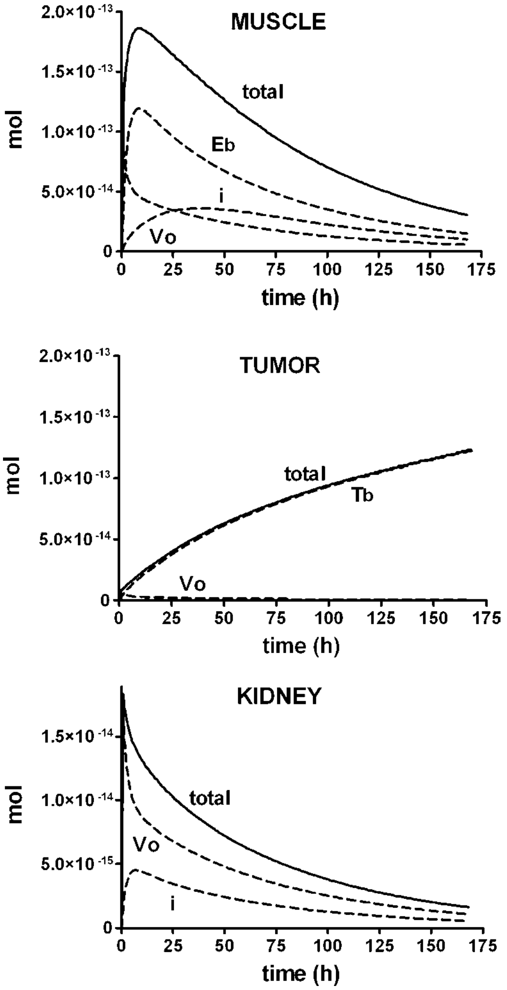

FIGURE 6. Predicted mAb distributions within compartments of muscle, tumor and spleen (total mAb (mol) vs. time). For tumor, virtually all antibody is predicted to be CEA-bound (T_b). For muscle, free endosomal antibody (E_f) is approximately zero. The amount of drug present in the vascular (V_o) space is roughly double the amount predicted to be in the interstitial (i_o) space in kidney and other two compartment organs. E_b represents endosomal, FcRn bound mAb. All predictions are made using Model B.

the concentration of mAb in *total* tumor (necrotic core plus perfusable mass).

We have shown that our new model can be used to describe the biodistribution of intact anti-CEA mAbs, as well as *predict* the biodistribution of $F(\mathrm{ab}')_2$ mAb fragments in mice. Addition of the FcRn and variable tumor mass submodels to Model A[4] resulted in an improved fit to the intact mAb data (Model B), with estimates of FcRn submodel parameters having %CV <14%, thereby permitting prediction of concentration-time profiles based on changes in IgG-FcRn binding rates. A lower %CV indicates that model output is more sensitive to changes in the associated parameter value, thus enabling a more accurate estimate of the parameter based on data fitting. The parameter %CVs reported in SAAM II are computed from the diagonal variance entries in the covariance matrix,[2] estimated using the unknown parameter sensitivity matrix.[43] Parameter sensitivities are thus implicit in %CV values reported. Table 2 shows that, in addition to FcRn submodel parameters, model output is sensitive to J_{iso} and L parameters for tumor, bone, kidney and lung (%CV < 64%). Model output is relatively insensitive to changes in J_{iso} and L parameters for GI tract and liver (%CV > 307%), most likely due to additional model complexity introduced by the hepatic portal system (Fig. 1).

Utilization of organ level biodistribution data (Fig. 4) coupled with a physiologically based description of mAb elimination and FcRn interaction (Fig. 1) enabled us to accurately estimate the rate of mAb internalization by endothelial cells ($k_{\mathrm{int,\,FcRn}} = 9.6 \times 10^{-3}\,\mathrm{min}^{-1}$, %CV = 12), subsequent degradation ($k_{\mathrm{deg,\,FcRn}} = 0.6127\,\mathrm{min}^{-1}$, %CV = 4) and recycling ($k_{\mathrm{rec,\,FcRn}} = 3.5 \times 10^{-3}\,\mathrm{min}^{-1}$, %CV = 14). Considering the high sensitivity of model output to changes in FcRn submodel parameters (low %CVs), successful prediction of the $F(\mathrm{ab}')_2$ biodistribution data (Fig. 4) suggests that these parameter estimates are physiologically meaningful and can be used to predict mAb biodistribution based on FcRn affinity. These results remain to be confirmed from laboratory measurements.

Other models have been proposed for describing mAb kinetics[4,12,20] and the FcRn system.[21] Ours extends these, for the first time integrating an organ specific FcRn submodel within a physiologically-based pharmacokinetic model, allowing successful prediction of mAb biodistribution based on FcRn affinity.

Current mAb dosing regimens for cancer treatment in humans are based primarily on empirical approaches,[31,51] which does not ensure optimal drug efficacy. Our new model is a step forward in the development of a whole-body pharmacokinetic model that can be used as a basis for computing optimal dosing regimes for drugs with varying FcRn affinity, thereby increasing the therapeutic power of anti-tumor monoclonal antibodies.

APPENDIX

MODEL EQUATIONS

Each flux arrow depicted in Fig. 1 is represented below using standard k_{ij} notation. For example, $k_{\mathbf{P},\mathbf{i_o}\_\mathbf{skin}}$ is the transfer coefficient, in units of min^{-1}, for mass flux from the interstitial compartment ($\mathbf{i_o}$) in the skin pool to the central plasma pool ($\mathbf{P}$). From Eq. A.1 below we see that $k_{\mathbf{P},\mathbf{i_o}\_\mathbf{skin}}$ has the following value:

$$
\begin{aligned}
k_{\mathrm{P},\mathbf{i_o}\_\mathrm{skin}} &= L_{\mathrm{skin}}/V_{\mathrm{i,skin}} = L_{\mathrm{skin,sp}}\mathrm{Mass}_{\mathrm{skin}}/V_{\mathrm{i,skin}} \\
&= 3.4 \times 10^{-6}\,\mathrm{ml\,min}^{-1}\,\mathrm{g}^{-1} \times 2.94\,\mathrm{g}/0.999\,\mathrm{ml} \\
&= 1 \times 10^{-5}\,\mathrm{min}^{-1}
\end{aligned}
$$

Note that lymph flow rate is given per unit mass, designated by the subscript sp. The total lymph flow rate for an organ is calculated by multiplying the specific flow rate by organ mass. *All k_{ij}'s are in units of* min^{-1}; all mass fluxes are in units of mol/min. State variables ($\mathbf{E_b}$, $\mathbf{E_f}$, $\mathbf{V_o}$, $\mathbf{i_o}$, $\mathbf{T_b}$ and $\mathbf{P}$) are shown in bold font and represent the number of moles of drug in a compartment at any give time. Compartment masses are converted to concentrations within equations when necessary.

Linear Mass Transfer Coefficients

The following transfer coefficients are constant throughout the course of the simulation, as shown above for $k_{\mathbf{P},\mathbf{i_o}\_\mathrm{skin}}$.

- Fractional lymph flow rate (labeled 'L' in Fig. 1):

$$k_{\mathbf{P},\mathbf{i_o}} = L_{\mathrm{organ}}/V_{\mathrm{i,organ}} \text{ (valid for tumor and all organs)} \tag{A.1}$$

- Fractional arterial plasma flow rate (labeled 'a' in Fig. 1):

$$k_{\mathbf{V_o}\_\mathrm{organ},\mathbf{P}} = Q_{\mathrm{organ}}/V_{\mathrm{plasma}} \times \text{(valid for all organs except lung, liver and tumor)} \tag{A.2a}$$

$$k_{\mathbf{V_o}\_\mathrm{lung},\mathbf{P}} = (Q_{\mathrm{lung}} - L_{\mathrm{lung}})/V_{\mathrm{v,lung}} \tag{A.2b}$$

$$k_{\mathbf{V_o}\_\mathrm{liver},\mathbf{P}} = (Q_{\mathrm{liver}} - Q_{\mathrm{GI}} - Q_{\mathrm{spleen}} + L_{\mathrm{GI}} + L_{\mathrm{spleen}})/V_{\mathrm{plasma}} \tag{A.2c}$$

- Fractional venous plasma flow rate (labeled 'v' in Fig. 1):

$$k_{\mathbf{V_o}\_\mathrm{lung},\mathbf{V}_{\mathrm{organ}}} = (Q_{\mathrm{organ}} - L_{\mathrm{organ}})/V_{\mathrm{v,organ}} \tag{A.3}$$

(valid for tumor and all organs)

- Fractional mAb elimination rate (labeled 'e' in Fig. 1):

$$k_{0,\mathbf{V_o}\_\mathrm{liver}} = k_{\mathrm{deg,liver}}/V_{v,\mathrm{liver}} \tag{A.4a}$$

$$k_{0,\mathbf{E_f}\_\mathrm{skin}} = k_{\mathrm{deg,FcRn}} \tag{A.4b}$$

$$k_{0,\mathbf{E_f}\_\mathrm{muscle}} = k_{\mathrm{deg,FcRn}} \tag{A.4c}$$

- Fractional mAb uptake rate by endothelial cells (labeled '*i*' in Fig. 1):

$$k_{\mathbf{E_{f\_skin}},\mathbf{V_{o\_skin}}} = k_{\text{int,FcRn}} \tag{A.5a}$$

$$k_{\mathbf{E_{f\_muscle}},\mathbf{V_{o\_muscle}}} = k_{\text{int,FcRn}} \tag{A.5b}$$

- Fractional mAb-receptor dissociation rate (labeled '*d*' in Fig. 1):

$$k_{\mathbf{i_{o\_tumor}},\mathbf{T_{b\_tumor}}} = k_{\text{off,CEA}} \tag{A.6a}$$

$$k_{\mathbf{E_{f\_skin}},\mathbf{E_{b\_skin}}} = k_{\text{off,FcRn}} \tag{A.6b}$$

$$k_{\mathbf{E_{f\_muscle}},\mathbf{E_{b\_muscle}}} = k_{\text{off,FcRn}} \tag{A.6c}$$

- Fractional mAb transport rate from endothelial cell to plasma (labeled '*r*' in Fig. 1):

$$k_{\mathbf{V_{o\_skin}},\mathbf{E_{b\_skin}}} = k_{\text{rec,FcRn}} \tag{A.7a}$$

$$k_{\mathbf{V_{o\_muscle}},\mathbf{E_{b\_muscle}}} = k_{\text{rec,FcRn}} \tag{A.7b}$$

Linear, Time-Varying Mass Transfer Coefficients

Linear, time-varying transfer coefficients are explicitly a function of time, i.e., $k_{i,j} = f(t)$.

- Fractional arterial plasma flow rate (labeled 'a_{TV}' in Fig. 1):

$$k_{\mathbf{V_{o\_tumor}},\mathbf{P}} = Q_{\text{tumor,sp}}\text{Mass}_{\text{tumor,perfusable}}/V_{\text{plasma}} \tag{A.8a}$$

$$\text{Mass}_{\text{tumor,perfusable}} = 0.4169(\text{Mass}_{\text{tumor}})^{0.62} \tag{A.8b}$$

Gompertz growth model

$$\text{Mass}_{\text{tumor}} = N_0 + C \times \exp(-\exp((2.718\,\mu/C) \times (\text{Lag} - t) + 1)) \tag{A.8c}$$

where $N_0 = 0.1868$ g, $C = 9.109$ g, $\mu = 0.000367$ g/min, Lag $= 11070$ min (Models *B* and $B_{\text{linear leaks}}$)$N_0 = 0.1460$ g, $C = 4.182$ g, $\mu = 0.0004715$ g/min, Lag $= 4325.4$ min (Model *C*).

Non-Linear Mass Transfer Coefficients

The nonlinear transfer coefficients in this model are functions of compartment masses.

- Fractional mAb-receptor binding rate (dashed arrows in Figure 1):

$$k_{\mathbf{E_{b\_skin}},\mathbf{E_{f\_skin}}} = k_{\text{on,FcRn}}(\text{FcRn}_{\text{tot}} - \mathbf{E_b}/V_{\text{endo}}) \tag{A.9a}$$

$$k_{\mathbf{E_{b\_muscle}},\mathbf{E_{f\_muscle}}} = k_{\text{on,FcRn}}(\text{FcRn}_{\text{tot}} - \mathbf{E_b}/V_{\text{endo}}) \tag{A.9b}$$

$$V_{\text{endo}} = V_{\text{v,organ}}(\mathbf{E}_{\text{b}}+\mathbf{E}_{\text{f}})/\mathbf{V}_{\text{o}} + \varepsilon \tag{A.9c}$$

set ε to 1×10^{-99} to avoid divide by zero at time 0 of simulation

$$k_{\mathbf{T_b},\mathbf{i_{o\_tumor}}} = k_{\text{on,CEA}}(B_{\max} - \mathbf{T_b}/V_{i,\text{tumor}}) \tag{A.10}$$

Two-Pore Extravasation Submodel

$$\begin{aligned} k_{\mathbf{i_o},\mathbf{V_o}} = {} & J_{L,\text{organ}}(1-\sigma_{\text{L}})/V_{\text{v,organ}} + \text{PS}_{L,\text{organ}} \\ & \times (1/V_{\text{v,organ}} - 1/V_{\text{i,organ}} \times \mathbf{i}_{\text{o}}/\mathbf{V}_{\text{o}}) \\ & \times \text{Pe}_{L,\text{organ}}/(e^{\text{Pe}_{L,\text{organ}}} - 1) \\ & + J_{S,\text{organ}}(1-\sigma_{\text{S}})/V_{\text{v,organ}} + \text{PS}_{\text{S,organ}} \\ & \times (1/V_{\text{v,organ}} - 1/V_{\text{i,organ}} \times \mathbf{i_o}/\mathbf{V_o}) \\ & \times \text{Pe}_{\text{S,organ}}/(e^{\text{Pe}_{\text{S,organ}}} - 1) \end{aligned} \tag{A.11a}$$

$$\text{Pe}_{\text{L,organ}} = (J_{\text{iso,organ}} + \alpha_{\text{L}}L_{\text{organ}})\frac{1-\sigma_E}{PS_{\text{L,organ}}}, \quad (\text{Pe} = \text{Peclet number}) \tag{A.11b}$$

(valid for tumor and all organs except kidney; for kidney, replace α_{L} with $\alpha_{\text{L, kidney}}$)

$$\text{Pe}_{\text{S,organ}} = (J_{\text{iso,organ}} + (1-\alpha_{\text{L}})L_{\text{organ}}) \times (1-\sigma_{\text{E}})/\text{PS}_{\text{S,organ}} \tag{A.11c}$$

(valid for tumor and all organs except kidney; for kidney, replace α_{L} with $\alpha_{\text{L, kidney}}$)

An Example

Using the above equations and Fig. 1, the differential equation for state variable $\mathbf{i_{o}}_{\text{\_tumor}}$ is written as follows:

$$\begin{aligned} \frac{d}{dt}(\mathbf{i_{o}}_{\text{\_tumor}}) = {} & k_{\mathbf{i_{o\_tumor}},\mathbf{T_b}}\mathbf{T_b} + k_{\mathbf{i_{o\_tumor}},V_{\mathbf{o\_tumor}}}V_{\mathbf{o}\text{\_tumor}} \\ & - k_{\mathbf{P},\mathbf{i}_{\text{tumor}}}\mathbf{i_{o}}_{\text{\_tumor}} - k_{T_{\mathbf{b}},\mathbf{i_{o\_tumor}}}\mathbf{i_{o}}_{\text{\_tumor}} \end{aligned} \tag{A.12}$$

All other equations are written similarly, with one equation for each compartment, 26 ODEs total.

Measurement Model

Experimental data is listed in units of percentage injected dose per gram of tissue (%ID/g) for each organ. We used the following measurement model for each organ pool in SAAM II during the fitting process:

$$\text{measured concentration of mAb in an organ} = 100\sum_{i=1}^{n}\mathbf{X}_i/(\text{dose} \times \text{Mass}_{\text{organ}}) \tag{A.13}$$

where $\mathbf{X}_i$ = amount of drug (mol) in compartment *i* at time *t*; *n* = number of compartments in organ pool. Note that for the central plasma pool measurement:

$$\text{Mass}_{\text{blood}} = \text{Mass}_{\text{plasma}}/(1 - \text{hematocrit}) \tag{A.14}$$

MODEL PARAMETERS

Drug Independent Parameters

$J_{\text{iso, bone, sp}} = 0.518 \times 10^{-4}\ \text{ml min}^{-1}\ \text{g}^{-1}$
$J_{\text{iso, heart, sp}} = 0.560 \times 10^{-4}\ \text{ml min}^{-1}\ \text{g}^{-1}$
$J_{\text{iso, liver, sp}} = 13.10 \times 10^{-4}\ \text{ml min}^{-1}\ \text{g}^{-1}$
$J_{\text{iso, muscle, sp}} = 0.050 \times 10^{-4}\ \text{ml min}^{-1}\ \text{g}^{-1}$
$J_{\text{iso, spleen, sp}} = 0.002 \times 10^{-4}\ \text{ml min}^{-1}\ \text{g}^{-1}$
$L_{\text{bone, sp}} = 3.037 \times 10^{-4}\ \text{ml min}^{-1}\ \text{g}^{-1}$
$L_{\text{heart, sp}} = 0.752 \times 10^{-4}\ \text{ml min}^{-1}\ \text{g}^{-1}$
$L_{\text{liver, sp}} = 64.50 \times 10^{-4}\ \text{ml min}^{-1}\ \text{g}^{-1}$
$L_{\text{muscle, sp}} = 0.757 \times 10^{-4}\ \text{ml min}^{-1}\ \text{g}^{-1}$
$L_{\text{spleen, sp}} = 1.111 \times 10^{-4}\ \text{ml min}^{-1}\ \text{g}^{-1}$
$k_{\text{deg, liver}} = 1.500 \times 10^{-4}\ \text{ml min}^{-1}$
$\text{Mass}_{\text{bone}} = 2.250\ \text{g}$
$\text{Mass}_{\text{heart}} = 0.133\ \text{g}$
$\text{Mass}_{\text{liver}} = 0.951\ \text{g}$
$\text{Mass}_{\text{muscle}} = 7.924\ \text{g}$
$\text{Mass}_{\text{skin}} = 2.940\ \text{g}$
$Q_{\text{bone}} = 0.171\ \text{ml min}^{-1}$
$Q_{\text{heart}} = 0.279\ \text{ml min}^{-1}$
$Q_{\text{liver}} = 1.103\ \text{ml min}^{-1}$
$Q_{\text{muscle}} = 0.792\ \text{ml min}^{-1}$
$Q_{\text{spleen}} = 0.050\ \text{ml min}^{-1}$
$V_{\text{plasma}} = 0.493\ \text{ml}$
$V_{\text{i, gi}} = 0.600\ \text{ml}$
$V_{\text{i, kidney}} = 0.101\ \text{ml}$
$V_{\text{i, lung}} = 0.057\ \text{ml}$
$V_{\text{i, skin}} = 1.000\ \text{ml}$
$V_{\text{i, tumor, sp}} = 0.547\ \text{ml g}^{-1}$
$V_{\text{v, gi}} = 0.100\ \text{ml}$
$V_{\text{v, kidney}} = 0.030\ \text{ml}$
$V_{\text{v, lung}} = 0.019\ \text{ml}$
$V_{\text{v, skin}} = 0.200\ \text{ml}$
$V_{\text{v, tumor,sp}} = 0.070\ \text{ml g}^{-1}$
$\text{FcRn}_{\text{tot}} = 4.00 \times 10^{-8}\ \text{mol ml}^{-1}$
$k_{\text{int, FcRn}} = 0.00961\ \text{min}^{-1}$
$k_{\text{off, FcRn}} = 0.03\ \text{min}^{-1}$
$B_{\text{max, sp}} = 8.30 \times 10^{-11}\ \text{mol ml}^{-1}$
$k_{\text{r, CEA}} = 8.46 \times 10^{-4}\ \text{min}^{-1}$

$J_{\text{iso, gi, sp}} = 3.033 \times 10^{-4}\ \text{ml min}^{-1}\ \text{g}^{-1}$
$J_{\text{iso, kidney, sp}} = 2.264 \times 10^{-4}\ \text{ml min}^{-1}\ \text{g}^{-1}$
$J_{\text{iso, lung, sp}} = 6.561 \times 10^{-4}\ \text{ml min}^{-1}\ \text{g}^{-1}$
$J_{\text{iso, skin, sp}} = 0.300 \times 10^{-4}\ \text{ml min}^{-1}\ \text{g}^{-1}$
$J_{\text{iso, tumor, sp}} = 6.274 \times 10^{-4}\ \text{ml min}^{-1}\ \text{g}^{-1}$
$L_{\text{gi, sp}} = 22.90 \times 10^{-4}\ \text{ml min}^{-1}\ \text{g}^{-1}$
$L_{\text{kidney, sp}} = 14.40 \times 10^{-4}\ \text{ml min}^{-1}\ \text{g}^{-1}$
$L_{\text{lung, sp}} = 8.509 \times 10^{-4}\ \text{ml min}^{-1}\ \text{g}^{-1}$
$L_{\text{skin, sp}} = 0.034 \times 10^{-4}\ \text{ml min}^{-1}\ \text{g}^{-1}$
$L_{\text{tumor, sp}} = 0.000\ \text{ml min}^{-1}\ \text{g}^{-1}$
$\text{Mass}_{\text{resto}} = 17.70\ \text{g}$
$\text{Mass}_{\text{gi}} = 3.450\ \text{g}$
$\text{Mass}_{\text{kidney}} = 0.298\ \text{g}$
$\text{Mass}_{\text{lung}} = 0.191\ \text{g}$
$\text{Mass}_{\text{blood}} = 0.758\ \text{g}$
$\text{Mass}_{\text{spleen}} = 0.100\ \text{g}$
$Q_{\text{gi}} = 0.897\ \text{ml min}^{-1}$
$Q_{\text{kidney}} = 0.799\ \text{ml min}^{-1}$
$Q_{\text{lung}} = 4.368\ \text{ml min}^{-1}$
$Q_{\text{skin}} = 1.205\ \text{ml min}^{-1}$
$\text{Q}_{\text{tumor, sp}} = 0.212\ \text{ml min}^{-1}\text{g}^{-1}$
$V_{\text{i,bone}} = 0.279\ \text{ml}$
$V_{\text{i, heart}} = 0.019\ \text{ml}$
$V_{\text{i, liver}} = 0.190\ \text{ml}$
$V_{\text{i, muscle}} = 1.030\ \text{ml}$
$V_{\text{i, spleen}} = 0.020\ \text{ml}$
$V_{\text{v, bone}} = 0.081\ \text{ml}$
$V_{\text{v, heart}} = 0.007\ \text{ml}$
$V_{\text{v, liver}} = 0.095\ \text{ml}$
$V_{\text{v, muscle}} = 0.151\ \text{ml}$
$V_{\text{v, spleen}} = 0.010\ \text{ml}$
$\alpha_{\text{L}} = 0.042$ (dimensionless)
$\alpha_{\text{L, kidney}} = 0.002$ (dimensionless)
$k_{\text{deg, FcRn}} = 0.613\ \text{min}^{-1}$
$k_{\text{rec, FcRn}} = 0.00345\ \text{min}^{-1}$
$k_{\text{f,CEA}} = 9.84 \times 10^{10}\ \text{ml min}^{-1}\ \text{mol}^{-1}$

Drug Dependent Parameters

$\sigma_{\text{L}} = 0.26$ (intact mAb), 0.11 [$F(\text{ab}')_2$] (dimensionless)
$\sigma_{\text{S}} = 0.98$ (intact mAb), 0.96 [$F(\text{ab}')_2$] (dimensionless)
$\text{P}_{\text{SL,sp}} = 2.66 \times 10^{-6}$ (intact mAb), 7.98×10^{-6} [$F(\text{ab}')_2$] $\text{ml min}^{-1}\ \text{g}^{-1}$
$\text{P}_{\text{SS,sp}} = 7.80 \times 10^{-6}$ (intact mAb), 2.34×10^{-6} [$F(\text{ab}')_2$] $\text{ml min}^{-1}\ \text{g}^{-1}$
$\text{k}_{\text{on,FcRn}} = 2.00 \times 10^{9}$ (intact mAb), 0 [$F(\text{ab}')_2$] $\text{ml min}^{-1}\ \text{mol}^{-1}$
$\text{Dose} = 8.30 \times 10^{-13}$ (intact mAb), 1.25×10^{-12} [$F(\text{ab}')_2$] mol

ACKNOWLEDGMENTS

The authors would like to thank Andrew Raubitschek, David Colcher, Sharon Hori and Owen Witte for their helpful advice and Larry Williams for providing additional biodistribution data. GZF was partially supported by the NIH Tumor Immunology Training Grant (5-T32-CA009120-28) and funds from Owen Witte and the Department of Microbiology, Immunology and Molecular Genetics.

REFERENCES

[1] Akaike, H. A new look at the statistical model identification. *IEEE Trans. Autom. Control* AC-19:716–723, 1974.

[2] Barrett, P. H., B. M. Bell, C. Cobelli, H. Golde, A. Schumitzky, P. Vicini, and D. M. Foster. SAAM II: Simulation, analysis, and modeling software for tracer and pharmacokinetic studies. *Metabolism* 47:484–492, 1998.

[3] Baxter, L. T., H. Zhu, D. G. Mackensen, W. F. Butler, and R. K. Jain. Biodistribution of monoclonal antibodies: Scale-up from

mouse to human using a physiologically based pharmacokinetic model. *Cancer Res.* 55:4611–4622, 1995.

[4]Baxter, L. T., H. Zhu, D. G. Mackensen, and R. K. Jain. Physiologically based pharmacokinetic model for specific and nonspecific monoclonal antibodies and fragments in normal tissues and human tumor xenografts in nude mice. *Cancer Res.* 54:1517–1528, 1994.

[5]Bell, B. M., J. V. Burke, and A. Schumitzky. A relative weighting method for estimating parameters and variances in multiple data sets. *Comput. Stat. Data. An.* 22:119–135, 1996.

[6]Berk, D. A., F. Yuan, M. Leunig, and R. K. Jain. Direct *in vivo* measurement of targeted binding in a human tumor xenograft. *Proc. Natl. Acad. Sci. U.S.A.* 94:1785–1790, 1997.

[7]Borvak, J., J. Richardson, C. Medesan, F. Antohe, C. Radu, M. Simionescu, V. Ghetie, and E. S. Ward. Functional expression of the MHC class I-related receptor, FcRn, in endothelial cells of mice. *Int. Immunol.* 10:1289–1298, 1998.

[8]Brambell, F. W., W. A. Hemmings, and I. G. Morris. A theoretical model of gamma-globulin catabolism. *Nature* 203:1352–1354, 1964.

[9]Brown, R. P., M. D. Delp, S. L. Lindstedt, L. R. Rhomberg, and R. P. Beliles. Physiological parameter values for physiologically based pharmacokinetic models. *Toxicol. Ind. Health* 13:407–484, 1997.

[10]Burmeister, W. P., A. H. Huber, and P. J. Bjorkman. Crystal structure of the complex of rat neonatal Fc receptor with Fc. *Nature* 372:379–383, 1994.

[11]Carter, P. Improving the efficacy of antibody-based cancer therapies. *Nat. Rev. Cancer* 1:118–129, 2001.

[12]Covell, D. G., J. Barbet, O. D. Holton, C. D. Black, R. J. Parker, and J. N. Weinstein. Pharmacokinetics of monoclonal immunoglobulin G1, $F(\mathrm{ab}')_2$, and Fab' in mice. *Cancer Res.* 46:3969–3978, 1986.

[13]Dedrick, R. L. Animal scale-up. *J. Pharmacokinet. Biopharm.* 1:435–461, 1973.

[14]Dias, S., K. Hattori, B. Heissig, Z. Zhu, Y. Wu, L. Witte, D. J. Hicklin, M. Tateno, P. Bohlen, M. A. Moore, and S. Rafii. Inhibition of both paracrine and autocrine VEGF/VEGFR-2 signaling pathways is essential to induce long-term remission of xenotransplanted human leukemias. *Proc. Natl. Acad. Sci. U.S.A.* 98:10857–10862, 2001.

[15]Fahey, J. L., and A. G. Robinson. Factors controlling serum gamma-globulin concentration. *J. Exp. Med.* 118:845–868, 1963.

[16]Fukumoto, T., M. R. Brandon. Importance of the liver in immunoglobulin catabolism. *Res. Vet. Sci.* 32:62–69, 1982.

[17]Gerlowski, L. E., and R. K. Jain. Physiologically based pharmacokinetic modeling: principles and applications. *J. Pharm. Sci.* 72:1103–1127, 1983.

[18]Ghetie, V., J. G. Hubbard, J. K. Kim, M. F. Tsen, Y. Lee, and E. S. Ward. Abnormally short serum half-lives of IgG in beta 2-microglobulin-deficient mice. *Eur. J. Immunol.* 26:690–696, 1996.

[19]Ghetie, V., and E. S. Ward. Transcytosis and catabolism of antibody. *Immunol. Res.* 25:97–113, 2002.

[20]Green, A. J., C. J. Johnson, K. L. Adamson, and R. H. Begent. Mathematical model of antibody targeting: important parameters defined using clinical data. *Phys. Med. Biol.* 46:1679–1693, 2001.

[21]Hansen, R. J., and J. P. Balthasar. Pharmacokinetic/pharmacodynamic modeling of the effects of intravenous immunoglobulin on the disposition of antiplatelet antibodies in a rat model of immune thrombocytopenia. *J. Pharm. Sci.* 92:1206–1215, 2003.

[22]Hefta, L. J., M. Neumaier, and J. E. Shively. Kinetic and affinity constants of epitope specific anti-carcinoembryonic antigen (CEA) monoclonal antibodies for CEA and engineered CEA domain constructs. *Immunotechnology* 4:49–57, 1998.

[23]Israel, E. J., V. K. Patel, S. F. Taylor, A. Marshak-Rothstein, and N. E. Simister. Requirement for a beta 2-microglobulin-associated Fc receptor for acquisition of maternal IgG by fetal and neonatal mice. *J. Immunol.* 154:6246–6251, 1995.

[24]Israel, E. J., D. F. Wilsker, K. C. Hayes, D. Schoenfeld, and N. E. Simister. Increased clearance of IgG in mice that lack beta 2-microglobulin: possible protective role of FcRn. *Immunology* 89:573–578, 1996.

[25]Jain, R. K. Delivery of novel therapeutic agents in tumors: physiological barriers and strategies. *J. Natl. Cancer Inst.* 81:570–576, 1989.

[26]Jones, E. A., and T. A. Waldmann. The mechanism of intestinal uptake and transcellular transport of IgG in the neonatal rat. *J. Clin. Invest.* 51:2916–2927, 1972.

[27]Junghans, R. P., and C. L. Anderson. The protection receptor for IgG catabolism is the beta2-microglobulin-containing neonatal intestinal transport receptor. *Proc. Natl. Acad. Sci. U.S.A.* 93:5512–5516, 1996.

[28]Keener, J. P., and J. Sneyd. Mathematical Physiology, 8th ed. New York: Springer, 1998, p. 766.

[29]Kim, J. K., M. Firan, C. G. Radu, C. H. Kim, V. Ghetie, and E. S. Ward. Mapping the site on human IgG for binding of the MHC class I-related receptor, FcRn. *Eur. J. Immunol.* 29:2819–2825, 1999.

[30]Ludwig, D. L., D. S. Pereira, Z. Zhu, D. J. Hicklin, and P. Bohlen. Monoclonal antibody therapeutics and apoptosis. *Oncogene* 22:9097–9106, 2003.

[31]Maloney, D. G., A. J. Grillo-Lopez, D. J. Bodkin, C. A. White, T. M. Liles, I. Royston, C. Varns, J. Rosenberg, and R. Levy. IDEC-C2B8: results of a phase I multiple-dose trial in patients with relapsed non-Hodgkin's lymphoma. *J. Clin. Oncol.* 15:3266–3274, 1997.

[32]Mink, J. G., J. Radl, P. van den Berg, J. J. Haaijman, M. J. van Zwieten, and R. Benner. Serum immunoglobulins in nude mice and their heterozygous littermates during ageing. *Immunology* 40:539–545, 1980.

[33]Nestorov, I. Whole body pharmacokinetic models. *Clin. Pharmacokinet.* 42:883–908, 2003.

[34]Ober, R. J., C. Martinez, C. Vaccaro, J. Zhou, and E. S. Ward. Visualizing the site and dynamics of IgG salvage by the MHC class I-related receptor, FcRn. *J. Immunol.* 172:2021–2029, 2004.

[35]Rastetter, W., A. Molina, and C. A. White. Rituximab: expanding role in therapy for lymphomas and autoimmune diseases. *Annu. Rev. Med.* 55:477–503, 2004.

[36]Riggs, D. S. The Mathematical Approach to Physiological Problems; A Critical Primer, 14th ed. Baltimore: Williams & Wilkins Co., 1963, p. 445.

[37]Riley, J. K., and M. X. Sliwkowski. CD20: A gene in search of a function. *Semin. Oncol.* 27:17–24, 2000.

[38]Rippe, B., and B. Haraldsson. Transport of macromolecules across microvascular walls: The two-pore theory. *Physiol. Rev.* 74:163–219, 1994.

[39]Rodewald, R., and J. P. Kraehenbuhl. Receptor-mediated transport of IgG. *J. Cell. Biol.* 99:159s–164s, 1984.

[40]Roopenian, D. C., G. J. Christianson, T. J. Sproule, A. C. Brown, S. Akilesh, N. Jung, S. Petkova, L. Avanessian, E. Y. Choi, D. J. Shaffer, P. A. Eden, and C. L. Anderson. The MHC class I-like IgG receptor controls perinatal IgG transport, IgG homeostasis, and fate of IgG-Fc-coupled drugs. *J. Immunol.* 170:3528–3533, 2003.

[41] Rubin, I., and Y. Yarden. The basic biology of HER2. *Ann. Oncol.* 12 Suppl 1:S3–S8, 2001.

[42] Rygaard, K., and M. Spang-Thomsen. Quantitation and gompertzian analysis of tumor growth. *Breast Cancer Res. Treat.* 46:303–312, 1997.

[43] Seber, G. A. F., and C. J. Wild. Nonlinear regression, 20th ed., Hoboken, NJ: Wiley-Interscience, 2003, p. 768.

[44] Sharkey, R. M., A. Natale, D. M. Goldenberg, M. J. Mattes. Rapid blood clearance of immunoglobulin G2a and immunoglobulin G2b in nude mice. *Cancer Res.* 51:3102–3107, 1991.

[45] Simister, N. E. Placental transport of immunoglobulin G. *Vaccine* 21:3365–3369, 2003.

[46] Theil, F. P., T. W. Guentert, S. Haddad, and P. Poulin. Utility of physiologically based pharmacokinetic models to drug development and rational drug discovery candidate selection. *Toxicol. Lett.* 138:29–49, 2003.

[47] Vaughn, D. E., and P. J. Bjorkman. High-affinity binding of the neonatal Fc receptor to its IgG ligand requires receptor immobilization. *Biochemistry* 36:9374–9380, 1997.

[48] Waldmann, T. A., and W. Strober. Metabolism of immunoglobulins. *Prog. Allergy* 13:1–110, 1969.

[49] Williams, L. E., R. B. Duda, R. T. Proffitt, B. G. Beatty, J. D. Beatty, J. Y. Wong, J. E. Shively, and R. J. Paxton. Tumor uptake as a function of tumor mass: A mathematic model. *J. Nucl. Med.* 29:103–109, 1988.

[50] Williams, L. E., A. M. Wu, P. J. Yazaki, A. Liu, A. A. Raubitschek, J. E. Shively, and J. Y. Wong. Numerical selection of optimal tumor imaging agents with application to engineered antibodies. *Cancer Biother. Radiopharm.* 16:25–35, 2001.

[51] Zhou, Y. Choice of designs and doses for early phase trials. *Fundam. Clin. Pharmacol.* 18:373–378, 2004.